Structural, electronic and adhesion characteristics of zinc/silica interfaces: ab initio study on zinc/β-cristobalite

Ha-Linh Thi Le, Jacek Goniakowski, Claudine Noguera, Alexey Koltsov, Jean-Michel Mataigne

Cite this: DOI: 10.1039/xxxxxxxxxx

Structural, electronic and adhesion characteristics of zinc/silica interfaces: ab initio study on zinc/β-cristobalite.

Ha-Linh Thi Le,[abc] Jacek Goniakowski,*[ab] Claudine Noguera,[ab] Alexey Koltsov,[c] and Jean-Michel Mataigne[c]

Received Date
Accepted Date

DOI: 10.1039/xxxxxxxxxx

www.rsc.org/journalname

The weak interaction between zinc and silica is responsible for a poor performance of anti-corrosive galvanic zinc coatings on modern advanced high strength steels. With the goal of identifying its microscopic origin, we report an extensive ab initio study of the structural, electronic, and adhesion characteristics of a variety of model zinc|β-cristobalite interfaces, representative for different oxidation conditions. We show that the weakness of the zinc-silica interaction at non polar interfaces is driven by the presence of surface siloxane rings. These latter are drastically detrimental to interface adhesion when intact and their breaking is impeded by a large energy barrier. Conversely, the characteristics of polar interfaces are principally driven by the capacity of zinc to screen the surface compensating charges and to form O-Zn bonds. This screening is especially efficient in oxygen-rich environment where the substrate-induced partial oxidation of the zinc deposit produces a considerable enhancement of interface adhesion. The identified microscopic mechanisms of interface interaction furnish precious guidelines towards practical attempts to improve adhesion. In particular, processes which enable breaking the surface siloxane rings are expected to noticeably reinforce the interaction at non-polar interfaces.

1 Introduction

For many years, adhesion to glass substrates has been the subject of intense studies because of its importance for the electronics industry. Today new challenges are faced also by the optimization of anti-corrosive galvanic zinc coatings on advanced high strength steels, where light strengthening elements (Al, Si and Mn) are alloyed with steel to meet the requirements of weight saving and CO_2 emission in the car and aircraft industries. The recrystallization annealing in a reducing atmosphere provokes a selective oxidation of these strengthening elements and the segregation of their oxides to the steel surfaces [1–4]. In particular, quasi-continuous amorphous silica films may form at the steel surface and reduce dramatically the adhesion of the zinc protection [5,6]. With the introduction of the new industrial process of Jet Vapor Deposition (JVD) of zinc under vacuum [7,8], a much better control of the industrial zinc/steel interface becomes possible. An assessment of zinc/silica interactions under different thermodynamic conditions will help to obtain a more precise understanding of the microscopic mechanisms responsible for the interfacial strength and to define appropriate process parameters promoting the adhesion of zinc coating on Si alloyed grades.

Surprisingly, while many theoretical studies have been dedicated to the adhesion of transition and noble metals on various oxide surfaces [9–13], the same is not true for silica. This may stem from the practical difficulty of simulating an amorphous interface, with many structural inhomogeneities and with no long range order. However, aside from its amorphous variety, SiO_2 possesses many cristalline polymorphs, among which α or β quartz, α or β cristobalite, and α or β tridymite, which are thermodynamically stable at normal pressure. They are all composed of corner-sharing oxygen tetrahedra around the Si atoms and may thus exhibit surface sites which locally bear resemblance to those of amorphous silica.

Information on several of these crystalline surfaces has been previously obtained with first principles methods, either by direct simulation of terminations [14,15] or by simulating dehydration of hydroxylated ones [16–18]. To our knowledge, the few existing first-principles simulations of metal/SiO_2 deal only with Cu/α-cristobalite [19], and with Ni, Al, or Pt interacting with quartz [20–22].

In the present study, we have chosen the β-cristobalite polymorph to mimic amorphous silica formed during the process of

[a] CNRS, Institut des Nanosciences de Paris, UMR 7588, F-75005 Paris, France. Fax: ; +33 (0)1 44 27 39 82 Tel: +33 (0)1 44 27 46 17; E-mail: Jacek.Goniakowski@insp.jussieu.fr
[b] Sorbonne Université, Institut des Nanosciences de Paris, UMR 7588, F-75005 Paris, France.
[c] ArcelorMittal Maizières Research, voie Romaine, F-57280, Maizières lès Metz, France.

steel recrystallization, because it forms at high temperatures and its atomic density is very close to that of amorphous silica. Such a strategy has already been adopted by other authors[16,18,23,24]. As to account for the various sites present at silica surfaces, we have considered two surface and interface orientations, namely (001) and (111), and we discuss their stability and their structural and electronic characteristics under various thermodynamic conditions (temperature and oxygen partial pressure). We show that the strength of the zinc/silica interface changes drastically as a function of interface stoichiometry and atomic structure. We analyze the microscopic processes at work at the interface and identify the most strongly interacting configurations.

The paper is organized as follows. After presenting the details and settings of the computational approach in Sec.2, we summarize the main characteristics of bare cristobalite surfaces of different orientation, stoichiometry and polar character (Sec.3). Results on interfaces with Zn are reported in Sec. 4, before a discussion (Sec. 5) and a conclusion.

2 Computational settings

All calculations are performed within the Density Functional Theory (DFT) implemented in VASP (Vienna ab initio simulation package)[25,26]. The interaction of valence electrons with ionic cores is described within the projector augmented wave (PAW) method[27,28]. The Kohn-Sham orbitals are developed on a plane-wave basis set with a cutoff energy of 400 eV and self-consistent iterative solution of the electronic Hamiltonian is pursued until energy differences become less than 10^{-6} eV. The dispersion-corrected GGA (optB86-vdW) exchange-correlation functional[29–31] is used to improve the description of adhesion characteristics, especially at weakly interacting zinc/SiO_2 interfaces. Atomic charges are estimated with the partition scheme proposed by Bader[32,33] and interface configurations are plotted with VESTA[34].

Bulk calculations Following the results and discussion in Ref.[35], the present study employs the I$\bar{4}$2d structural variant of β-cristobalite. We find that with a Γ-centered 6×6×6 Monkhorst-Pack grid the calculated structural characteristics (lattice parameters, bond lengths, and angles) are converged to within 0.01 Å and 0.01°, respectively, and the formation energies are converged to 0.01 eV/SiO_2. Results, summarized in Tab. 1, are in a good overall agreement with experimental bulk characteristics.

Surface calculations In order to account for the various sites present at silica surfaces we consider the (001) and (111) surfaces of β-cristobalite, which are characterized by different orientations of the surface SiO_4 tetrahedra and by a different coordination of surface Si atoms, Figure 1. Since the surface polar character of both orientations depends on the precise surface termination[38], for each of them we consider three qualitatively different terminations: polar oxygen-lean and oxygen-rich, and non-polar stoichiometric ones, Figure 1. In the following, we will label them according to their surface stoichiometry, with respect to a neutral dipole-free repetitive bulk unit cell[38]: SiO (O-lean), SiO_2 (stoichiometric), and SiO_3 (O-rich). Along the (001) orientation, the repetitive unit cell is composed of a O/Si/O sequence of atomic layers, so that the smallest surface unit cell (with a single surface cation) can be used to represent the non-polar termination. Conversely, since for the (111) orientation the repetitive unit cell is composed of a $O_{0.5}/Si_2O_3/O_{0.5}$ layer sequence, a larger unit cell with two surface cations is needed. For both orientations, a compensating charge of two electrons or two holes per surface unit cell is necessary to heal the polarity of O-lean and O-rich terminations, respectively.

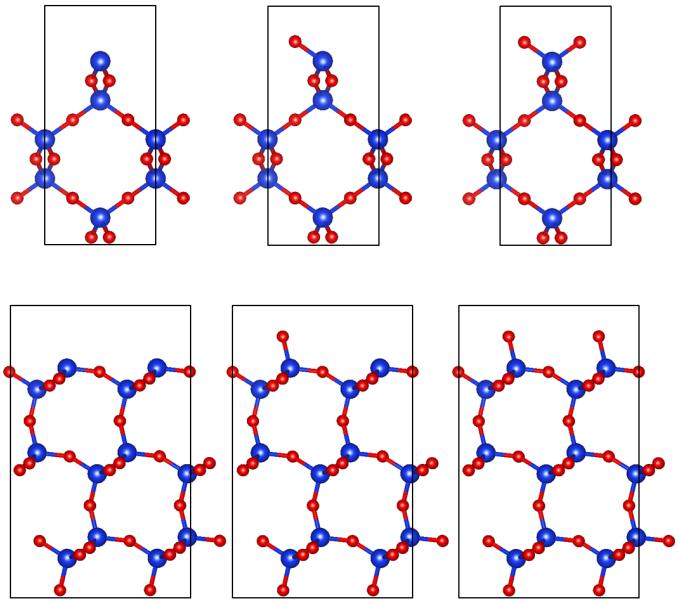

Fig. 1 Unrelaxed (bulk-cut) terminations of the (001) (top) and (111) (bottom) surfaces of β-cristobalite. From left to right: oxygen-lean (SiO), stoichiometric (SiO_2), and oxygen-rich (SiO_3). Si and O atoms are represented by large blue and medium red balls, respectively. Surface unit cells for each orientation are indicated.

All surfaces are modeled with slabs separated by at least 10 Å of vacuum and dipole corrections[25,39] are used to further attenuate the effect of periodic boundary conditions in the direction normal to the slab surfaces. As to limit the structural distortions within the SiO_2 slabs and to improve the convergence with respect to their thickness, we use asymmetric slabs with one bare termination and one fully hydroxylated. Except for the surface Si atoms at the hydroxylated terminations which are kept fixed, all other atoms are relaxed until forces become smaller than 0.01 eV/Å^2. Consistently with bulk tests, 6×6×1 and 6×12×1 k-point samplings are used for the (001) and (111) surfaces, respectively. With such settings 9 and 5 SiO_2 layers, respectively, are sufficient to obtain surface energies converged to within 0.01 J/m^2.

The total surface energy of the asymmetric slabs is the sum of surface energies of their bare σ_{SiO_x} and their hydroxylated σ_{SiOH} terminations:

$$\sigma_{SiO_x} + \sigma_{SiOH} = \frac{E^{a-slab} - E^{bulk}_{SiO_2} - nE_{H_2O} - \Delta N_O \mu_O}{S} \qquad (1)$$

where E^{a-slab}, $E^{bulk}_{SiO_2}$, and E_{H_2O} are the total energies of the asymmetric slab, of bulk SiO_2, and of a free water molecule, respectively. ΔN_O gives the excess/deficiency of oxygen atoms in the slab with respect to the SiO_2 ($+nH_2O$) stoichiometry, μ_O

Table 1 Calculated and experimental characteristics of bulk I$\bar{4}$2d β-cristobalite: lattice parameter a (Å) and c/a ratio, Si-O bond lengths (Å), O-Si-O and Si-O-Si bond angles (°), formation energy per oxygen atom E^{form} (eV) referred to bulk silicon and to a free oxygen molecule, and the corresponding experimental value of standard formation enthalpy $\Delta_f H^\circ$ (eV) from Refs. 36,37.

	a (Å)	c/a	Si-O (Å)	O-Si-O (°)	Si-O-Si (°)	E^{form} (eV)
GGA-vdW	6.94	1.06	1.63	108.6/111.3	140.7	4.7
Exp.	7.13	1.00	1.61	107.8/112.9	146.7	4.7

is the oxygen chemical potential, and S is the surface unit cell area. Since the evaluation of σ_{SiO_x} requires the knowledge of $\sigma_{SiOH} = (E^{s-slab} - E^{bulk}_{SiO_2} - 2nE_{H_2O})/2S$, the total energy E^{s-slab} of a symmetric stoichiometric cristobalite slab with both terminations equivalently hydroxylated is also calculated.

The surface energy σ_{SiO_x} depends on the stoichiometry of the surface termination quantified by ΔN_O and on the oxygen chemical potential μ_O. The latter is conventionally referred to the total energy E_{O_2} of a free oxygen molecule: $\mu_O = \frac{1}{2}E_{O_2} + \Delta\mu_O$, such that $\Delta\mu_O \sim 0.0$ eV corresponds to oxygen-rich conditions (condensation of oxygen molecules) and $\Delta\mu_O = (E^{bulk}_{SiO_2} - E^{bulk}_{Si} - E_{O_2})/2 \sim -4.7$ eV (E^{bulk}_{Si} is the total energy of bulk silicon) describes an extremely oxygen-poor environment (decomposition of bulk SiO_2). Oxygen chemical potential can be explicitly linked to oxygen thermodynamic conditions (oxygen partial pressure p_O and temperature T): $\Delta\mu_O(T, p_O) = \Delta\mu_O(T, p_0) + \frac{1}{2}kT \ln\frac{p_O}{p_0}$.

Interface calculations The simulations of zinc/SiO_2 interfaces make use of the asymmetric SiO_2 slabs with zinc films deposited on their bare terminations. Periodic images are separated by a vacuum layer of at least 10 Å and dipole corrections are systematically applied. In all cases the in-plane lattice parameters are fixed to those of the bare SiO_2 surface and the zinc is laterally distorted as to match the SiO_2 lattice. In order to reduce mismatch effects, we have used (2×1)-Zn(0001)‖(1×1)-SiO_2(001) and (4×2)-Zn(0001)‖(1×1)-SiO_2(111) coincidence cells. The resulting interface mismatch $(a_{Zn} - a_{SiO_2})/a_{Zn}$ along the two in-plane directions a and b is equal to +7% and -7% in the first case and +7% and +4% in the second one. We have verified that despite the distortion, the zinc deposits preserve their hexagonal lattice and (0001) orientation and that their surface energies σ_{Zn} is modified by less than 0.2 J/m^2. We have systematically used 9 zinc layers, which assures a convergence of surface and interface energies to within 0.01 J/m^2. In all calculations, the positions of all atoms (except for the surface silicon atoms at the hydroxylated slab termination) are relaxed until residual forces become smaller than 0.01 eV/Å. The most stable interface configurations are obtained from a series of independent optimizations, starting from various interface registries between the two lattices.

The interface strength is estimated from the separation energy $E^{sep} = (E^{a-slab} + E_{Zn\text{-}E_{Zn/SiO_x}})/S$, where E_{Zn/SiO_x}, E^{a-slab}, and E_{Zn} are the total energies of the Zn/SiO_x heterostructure and of the isolated silica and Zn slabs with the same in-plane lattice parameters. The interface stability is estimated from the interface energy $E^{int} = \sigma_{SiO_x} + \sigma_{Zn} - E^{sep}$.

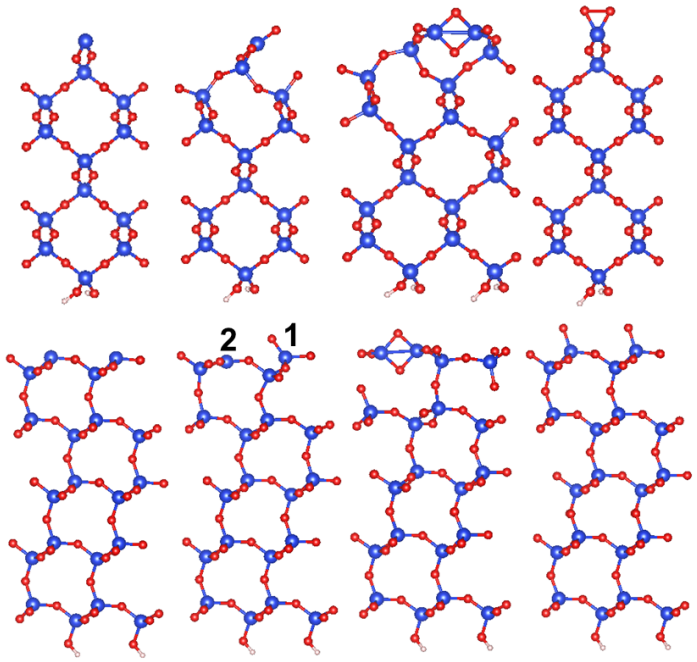

Fig. 2 Relaxed structures of the alternative terminations of the (001) (top) and (111) (bottom) surfaces. Left to right: SiO, SiO_2, D_2-SiO_2, and SiO_3 terminations. Si, O, and H atoms are represented by large blue, medium red, and small white balls, respectively.

3 The bare (001) and (111) β-cristobalite surfaces

As shown in Fig. 2, the trends in structural relaxation are very similar on the (001) and (111) surfaces. At the polar SiO terminations, relaxation effects are relatively weak and the atomic structures are close to the corresponding bulk cuts. At the stoichiometric SiO_2 terminations, two qualitatively different surface configurations can be found. The first one (labeled SiO_2) bears a close resemblance to the unrelaxed structure aside from an important flattening of the outermost SiO_3 entity around the undercoordinated surface Si. The second one (labeled D_2-SiO_2) results from a more thorough rearrangement of surface atoms and contains two-membered silica rings (D_2 siloxane rings). Only at the polar SiO_3 terminations the surface structures of the two orientations quantitatively differ. While relaxation effects are relatively small at the (111) surface, a surface O_2 complex, with a short O-O bond forms at the (001) surface.

The main electronic characteristics of these surfaces, summarized in Tab. 2 and in Fig. 3 are strongly dependent on the surface polar character. On the polar SiO terminations, the two excess electrons (per surface unit cell) required for polarity com-

Table 2 Electronic characteristics of the four terminations of the (001) and (111) surfaces: band gaps (E_g) and Bader charges of surface silicon and oxygen atoms (Q_{Si}, Q_O). Corresponding results for bulk β-cristobalite are given for reference.

	SiO	SiO_2	D_2-SiO_2	SiO_3	bulk
(001)					
Q_{Si} (e)	1.80	2.96	3.13 (×2)	3.08	3.18
Q_O (e)	-	-1.25	-1.56 (×2)	-0.65 (×2)	-1.59
E_g (eV)	3.20	3.78	5.30	2.25	5.83
(111)					
Q_{Si} (e)	2.40 (×2)	3.09, 3.20	3.19 (×2)	3.14 (×2)	3.18
Q_O (e)	-	-1.30	-1.33, -1.80	-0.80 (×2)	-1.59
E_g (eV)	1.61	1.32	5.49	0.00	5.83

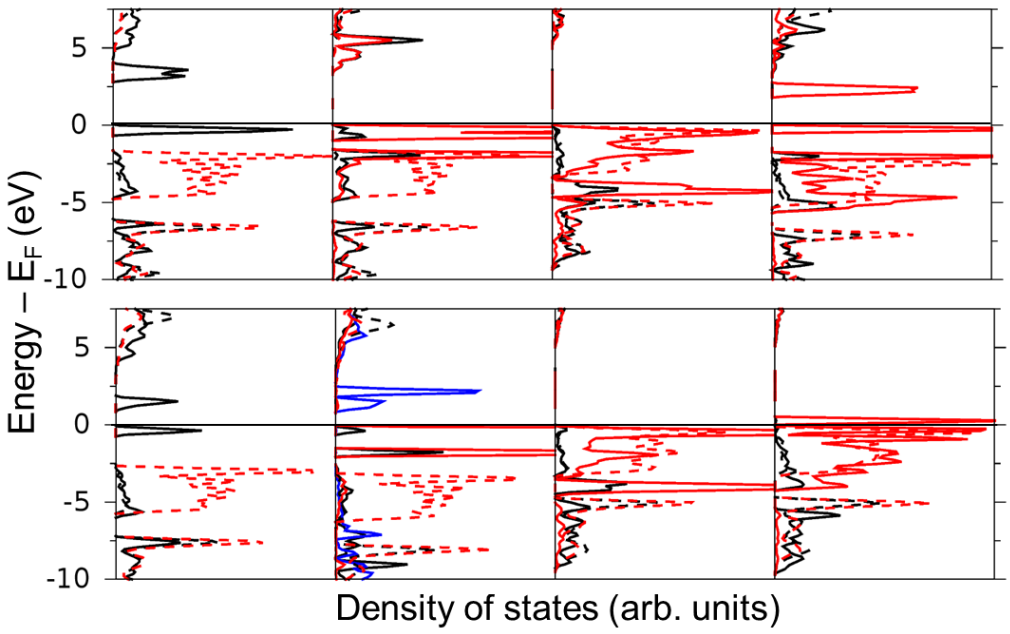

Fig. 3 Local density of states (LDOS) projected on surface (full lines) and bulk (dashed lines) cations (black and blue) and anions (red) at the four terminations (left to right: SiO, SiO_2, D_2-SiO_2, and SiO_3) of the (001) (top) and (111) (bottom) surfaces of β-cristobalite. LDOS of cations labeled 1 and 2 in Fig. 2 are plotted in black and blue, respectively.

pensation are localized on the under-coordinated surface Si and partially fill-up empty conduction band states. Due to the different number of surface cations per unit cell, this results in Si^{+2} and Si^{+3} formal oxidation states at the (001) and (111) surfaces, respectively, with non-vanishing spin moments on the surface cations in the latter case. A substantial reduction of the gap width occurs, separating filled and empty states of surface Si character, Fig. 3.

On the polar SiO_3 terminations, the two excess holes (per surface unit cell) required for polarity compensation are accommodated by the under-coordinated surface anions. At the (001) surface the two anions form a surface peroxo group with a formal O_2^{2-} charge state, which yields a substantial decrease of the band gap (between the filled and empty states of the peroxo group, Fig. 3). At the (111) surface, no such complex forms, so that the two surface anions are in a formal O^- spin-polarized state and the surface band gap is closed, Fig. 3.

At the non-polar stoichiometric terminations, the modifications of the electronic structure are also quite important despite the absence of electron excess or deficiency. In the SiO_2 configurations, an sp^2-like hybridization takes place around the under-coordinated Si with an enhanced covalency of the Si-O bonds. As a consequence, the surface oxygen charges are somewhat smaller than in the bulk and the band gaps are significantly reduced. With respect to the SiO_2 configurations, the formation of surface siloxane rings (D_2-SiO_2 configurations) increases the coordination of the surface anions, reestablishes their average bulk-like charges, and enables a substantial gap opening, Fig. 3.

Surface energies reported in Fig. 4 allow comparison of stability between all surface terminations as a function of oxygen conditions. The general trends are again very similar for the two surface orientations. Systematically, polar terminations are stable only in extremely O-rich (SiO_3) or extremely O-lean (SiO) environments, due to the large energy cost to accommodate the compensating surface charges. Consistently with the microscopic mechanisms discussed above, the accommodation of excess electrons costs somewhat less energy at the (001) surface, while the electron deficiency is accommodated more easily by the (111) one. Surface configurations with siloxane rings (D_2-SiO_2) are systematically by far the most stable surface terminations over a wide range of oxygen conditions accessible experimentally, Fig. 4, which is consistent with the absence of broken surface bonds and with their bulk-like electronic structure.

Thus, consistently with the existing experimental and theoretical evidence [14,18,40–42], surface siloxane rings turn out to be characteristic of stable silica surfaces. In Tab. 3 we compare the detailed characteristics of three alternative D_2 configurations obtained in the present study. While a single one is found at the (001) surface, two different ones can be formed at the (111) surface, with D_2 rings oriented along the surface *a* [D_2-$SiO_2(111)_I$] or *b* [D_2-$SiO_2(111)_{II}$] vectors, respectively. The former, represented in Figure 2, is slightly more stable. The latter was shown to form upon (simulated) dehydroxylation of the cristobalite (111) surface, Ref. 18. We find that the structural characteristics of the three siloxane groups are quasi-identical and that cation and average anion charges are similarly bulk-like, which proves a rela-

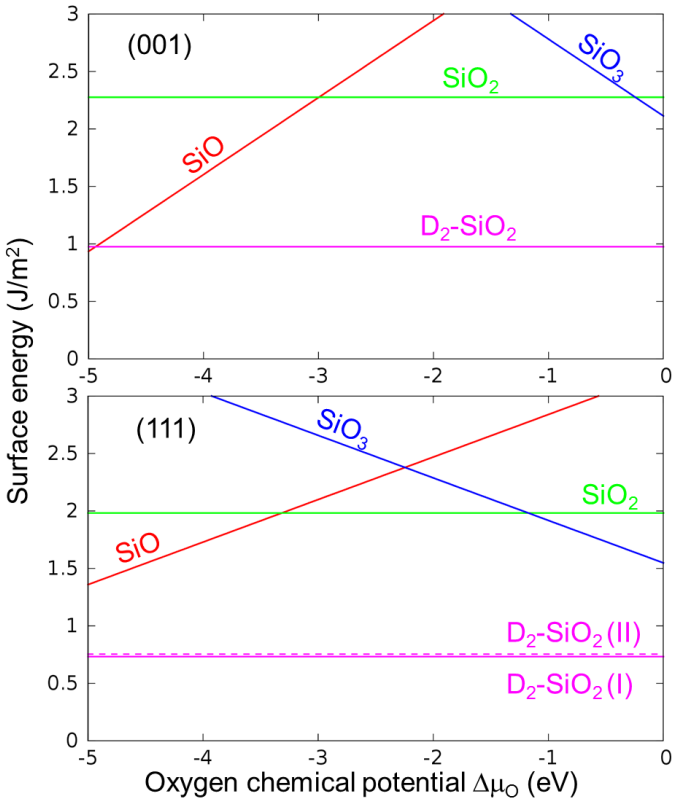

Fig. 4 Calculated surface energies of the various terminations of the β-cristobalite (001) (top) and (111) (bottom) surfaces as a function of the oxygen chemical potential $\Delta\mu_O$.

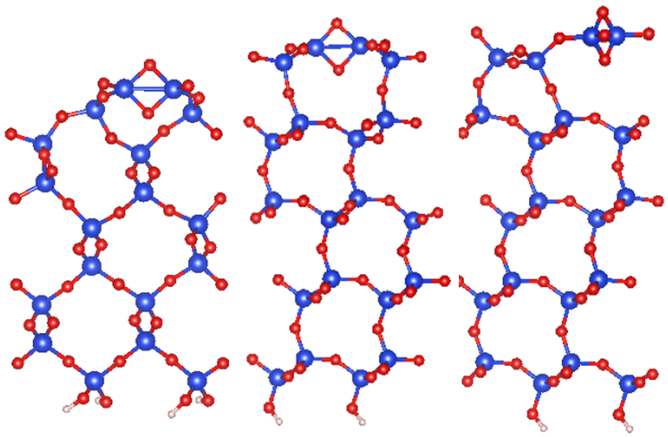

Fig. 5 Atomic structure of surface siloxane groups. From left to right: D_2-$SiO_2(001)$, D_2-$SiO_2(111)_I$, and D_2-$SiO_2(111)_{II}$ configurations. Si, O, and H atoms are represented by large blue, medium red, and small white balls, respectively.

tively small impact of the local crystal structure on the ring characteristics. We note however that while, in the (001) rings, the charges of the two anions are equal, they visibly differ at the (111) surface, suggesting a more covalent character of the outermost Si-O_1 bonds. Finally, while the formation energies of the two (111) D_2 rings are very similar, the small E^{form} difference between the (001) and (111) surfaces can be assigned to the different structures and stability of the corresponding SiO_2 configurations.

Table 3 Structural, electronic, and energetic characteristics of siloxane rings D_2-SiO_2 at (001) and (111)-oriented surfaces. Formation energies E^{form} are referred to the corresponding SiO_2 surface configurations.

	(001)	$(111)_I$	$(111)_{II}$
Si-O (Å)	1.68	1.68	1.68
Si-O-Si (°)	89.35	89.92	90.02
Q_{Si} (e)	3.13 (×2)	3.19 (×2)	3.21 (×2)
Q_{O_1} (e)	-1.56	-1.33	-1.33
Q_{O_2} (e)	-1.56	-1.80	-1.81
E^{form} (eV)	-3.89	-3.37	-3.32

To summarize, we find that the polar (001) and (111) terminations of β-cristobalite surfaces are systematically unstable under accessible oxygen conditions. The most favored non-polar configurations involve D_2 siloxane rings whose characteristics show a relatively small dependence on surface orientation and local structure. The present cristobalite-based surface models may thus satisfactorily account for the properties of the two-membered siloxane rings which have been identified at amorphous SiO_2 surfaces.

4 Zinc/β-cristobalite interfaces

Figure 6 shows the optimized structures of zinc in contact with the various (001) and (111) terminations of β-cristobalite and highlights the Zn-O and Zn-Si bonds formed at the interface. The corresponding atom-projected densities of states and interfacial atomic charges are summarized in Figure 7 and Table 4, respec-

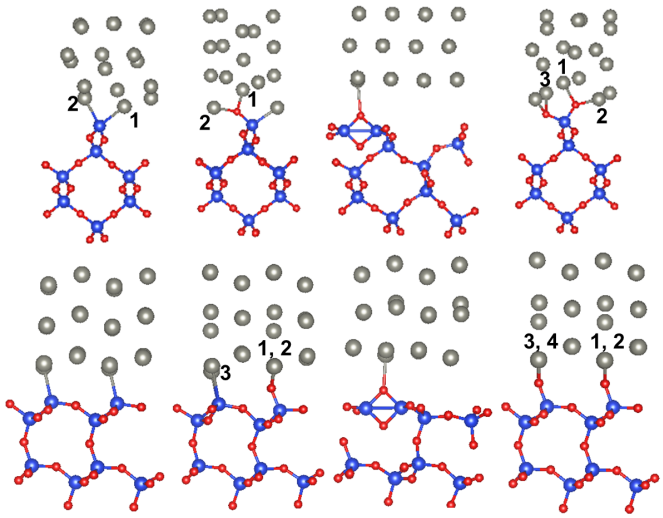

Fig. 6 Atomic structures of various (001) (top) and (111) (bottom) Zn/β-cristobalite interfaces. Left to right: Zn/SiO, Zn/SiO_2, Zn/D_2-SiO_2, and Zn/SiO_3 interfaces. Si, Zn, and O are shown with large blue, large gray, and medium red balls, respectively. Interfacial Zn-O and Zn-Si bonds are explicitly drawn.

tively. Several generic features, which are independent of the substrate orientation can be pointed out.

On the one hand, each singly-coordinated surface oxygen tends to form two O-Zn bonds, inducing an electron transfer from zinc to oxygen (about 0.3-0.4 e/bond) and a partial ionization of the interfacial zinc atoms, Tab. 4. The strongest effect occurs at the Zn/SiO_3 interfaces, where the density of surface oxygen is the highest and where the largest proportion of interfacial Zn becomes partially ionized. Conversely, the two-fold coordinated oxygen atoms belonging to the siloxane rings (Zn/D_2-SiO_2) form a single O-Zn bond, associated with a much smaller electron transfer (about 0.1-0.2 e/bond), Tab. 4. On the other hand, surface silicon atoms tend to recover their full tetrahedral environment by forming additional Si-Zn bonds with a systematically small electron transfer (less than 0.1 e, Tab. 4).

The resulting electronic properties strongly depend on the stoichiometry and surface configuration of the cristobalite substrate. In the polar Zn/SiO LDOS, the formation of Si-Zn bonds suppresses the localized Si states present at the bare SiO surface and produces a wide hybridized Si-Zn band which overlaps the whole gap, Fig. 7. The very small electron transfer across this interface indicates that the compensating charges are very weakly screened by the zinc deposit and, as at the bare SiO surfaces, the excess electrons remain predominantly localized on the surface Si. Conversely, at polar Zn/SiO_3 interfaces, the zinc deposit very efficiently screens the hole excess necessary to compensate the surface polarity. Indeed, the peroxo groups present at the bare (001) surface are broken and for both substrate orientations a substantial electron transfer from Zn towards the oxide enables all surface anions to recover their bulk-like (O^{2-}) oxidation state, Tab. 4. As a consequence, the oxide substrate becomes quasi-insulating, with only metal-induced gap states in its gap, Fig. 7.

Among the two non-polar terminations, the metal-induced

Table 4 Calculated charges (per surface unit cell) of interfacial silicon, oxygen, and zinc atoms at the four considered (001) and (111) interfaces. Zinc charges are given in the order given by labels in Fig. 6.

	SiO/Zn	SiO_2/Zn	D_2-SiO_2/Zn	SiO_3/Zn
(001)				
Q_{Si} (e)	1.57	2.31	3.13 (×2)	3.16
Q_O (e)	-	-1.40	-1.53, -1.62	-1.34, -1.44
Q_{Zn} (e)	0.10, -0.04	0.38, 0.43	0.13	0.30, 0.67, 0.34
(111)				
Q_{Si} (e)	2.52 (×2)	3.16, 2.35	3.19 (×2)	3.17 (×2)
Q_O (e)	-	-1.38	-1.47, -1.74	-1.36 (×2)
Q_{Zn} (e)	-0.05 (×2)	0.32, 0.34, 0.10	0.18	0.34 (×4)

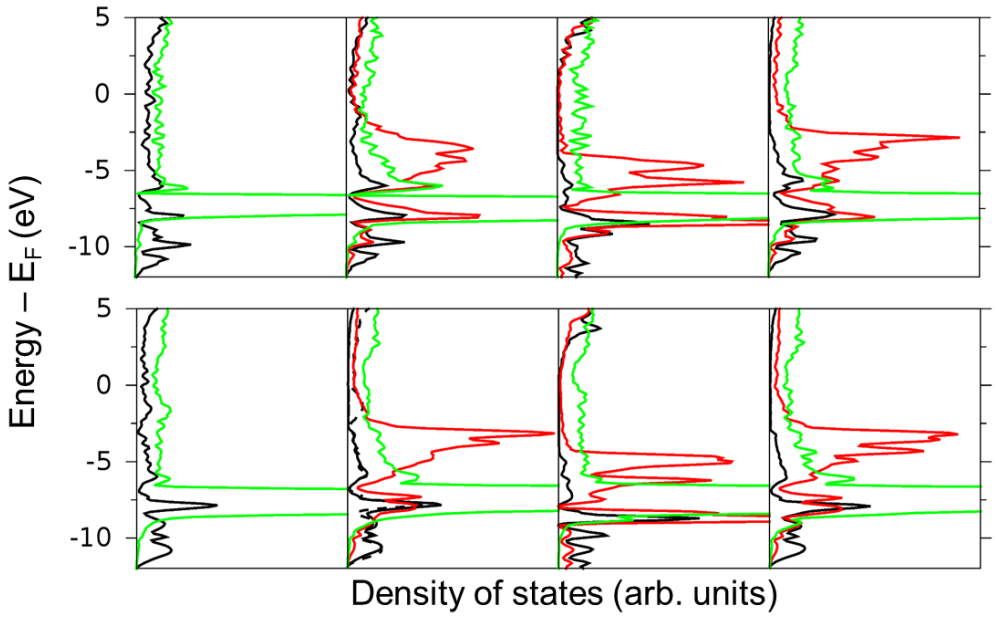

Fig. 7 Local density of states projected on interfacial atoms: Si (black lines), O (red lines) and Zn (green lines) atoms at (001) (top) and (111) (bottom) interfaces. From left to right: Zn/SiO, Zn/SiO_2, Zn/D_2-SiO_2, and Zn/SiO_3.

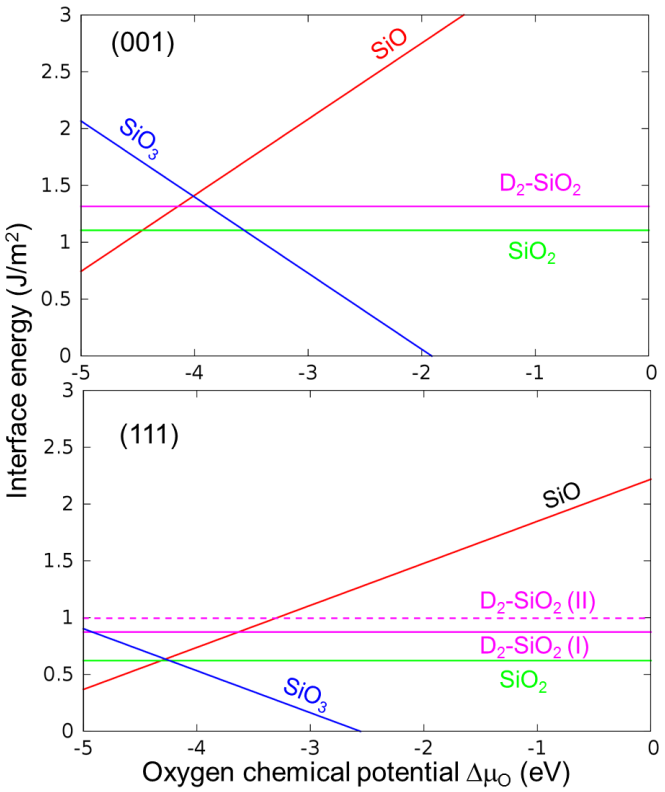

Fig. 8 Calculated interface energies of the Zn/β-cristobalite (001) (top) and (111) (bottom) interface configurations as a function of the oxygen chemical potential $\Delta\mu_O$.

modifications are the weakest at the Zn/D_2-SiO_2 interfaces, where the siloxane rings remain intact, and a low density of relatively weak O-Zn bonds is formed. The surface is insulating and only metal-induced gap states are present in the gap region, Fig. 7. The case of Zn/SiO_2 interfaces is of a particular interest since, despite its non-polar character, a non-negligible electron transfer from Zn towards the oxide substrate takes place. While this electron transfer is mediated by the interfacial O-Zn bonds, it mainly impacts the surface Si charge, Tab. 4. This finding suggests a competition between O-Si and O-Zn bonds at the interface and points towards a possible stabilization of interfacial Si^{3+} species by a partial ionization of zinc atoms.

Figure 8 displays the relative stability of the (001) and (111) Zn/β-cristobalite interfaces as a function of the oxygen chemical potential $\Delta\mu_O$. Independently of the interface orientation, the zinc deposit induces dramatic changes compared to the bare cristobalite surfaces, Fig. 4. Firstly, the polar terminations are substantially stabilized. The polar Zn/SiO_3 interface, at which zinc becomes positively charged, is thermodynamically favored over a wide span of oxygen-intermediate and oxygen-rich conditions and the polar Zn/SiO one is only stable in an extremely oxygen-lean environment. As a consequence the stability range of the non-polar interfaces is largely reduced and even practically vanishing in the case of the (111) orientation. Secondly, the relative stability of the two non-polar terminations is reversed. The formation of a larger number of stronger O-Zn bonds at the Zn/SiO_2 interfaces produces a stabilizing effect which overrides the energy gain of the siloxane ring formation at the bare SiO_2 surface.

Table 5 Separation energies E^{sep} (J/m^2) of various (001) and (111) zinc/silica interfaces.

E^{sep}	SiO	SiO_2	D_2-SiO_2	SiO_3
(001)	0.83	1.81	0.30	4.03
(111)	1.90	2.00	0.50	3.41

Separation energies E^{sep} at Zn/cristobalite interfaces are summarized in Tab. 5. As for the interface energies, the trends are very similar for the two interface orientations. The largest E^{sep} are obtained at the polar O-rich interfaces (Zn/SiO_3) as a result of the efficient screening of polarity by the metal and of the high density of interfacial O-Zn bonds. Conversely, the quasi-absence of metal screening and the absence of O-Zn bonds in the case of polar O-lean interfaces (Zn/SiO) result in much smaller separation energies. For the two non-polar interfaces, E^{sep} is moderately large at the SiO_2 terminations, consistently with a relatively large number of strong O-Zn bonds (large electron transfer). It is particularly small at the Zn/D_2-SiO_2 interface, because the presence of the siloxane rings allows only few weak O-Zn bonds to be formed. This suggests that cleavage will be cohesive inside Zn in the former case and interfacial in the latter one.

In summary, we show that the characteristics of zinc/cristobalite interfaces depend relatively little on their orientation, but are very sensitive to their precise structure and composition. On the one hand, the O-rich and O-lean polar terminations behave very differently, principally due to a good capacity of zinc to provide compensating electrons and to form numerous O-Zn bonds at the O-rich (Zn/SiO_3) interfaces, compared to no electron uptake by zinc and uniquely Si-Zn bonds at the O-lean (Zn/SiO) ones. As a consequence, while the two types of polar terminations are stabilized by the zinc deposit, the effect is much more significant for the SiO_3 terminations, which become the most stable over a wide range of moderate and rich oxygen conditions, and are characterized by a strong adhesion. On the other hand, the characteristics of non polar interfaces substantially depend on the interface structure. While the oxygen atoms belonging to the siloxane rings (D_2-SiO_2) interact weakly with the zinc deposit, with virtually no modification of the surface electronic structure, the under-coordinated oxygen atoms at the SiO_2 terminations form several iono-covalent O-Zn bonds accompanied by a non-negligible interfacial charge transfer. This produces moderately strong interfaces with Si^{3+} species stabilized by a partial zinc ionization. As a consequence, compared to bare surfaces, the relative stability of the two non-polar terminations is reversed. While siloxane-terminated surfaces are by far favored in contact with vacuum, they become thermodynamically less stable than the SiO_2 terminations in the presence of zinc deposit.

5 Discussion

The computational results enable an identification of two generic configurations in which the zinc-silica interaction is strong. The

first one is the polar O-rich Zn/SiO_3 interface, at which adhesion is driven by the good capacity of zinc to provide compensating electrons and to form numerous interfacial O-Zn bonds. Although energetically very promising, this interface configuration may be relatively difficult to obtain by deposition of zinc on silica surfaces due to the instability of the bare polar O-rich SiO_3 termination. The second is the non-polar Zn/SiO_2 interface where strong covalent O-Zn bonds are formed. In the following we scrutinize this interface configuration as to better asses its actual interest for anti-corrosive zinc coatings.

At non-polar zinc/silica interfaces two configurations compete: the siloxane-terminated surfaces D_2-SiO_2 which are energetically favored when bare, and the SiO_2 configurations with broken siloxane rings, which are the most stable in the presence of zinc. The latter display separation energies of 1.8 - 2.0 J/m^2, significantly larger than the one inside the zinc deposit (1.1 J/m^2), which makes them promising for applications in anti-corrosive zinc coatings. However, according to our calculations, the siloxane rings at zinc/silica interfaces do no break spontaneously and the resulting meta-stable interface configurations (Zn/D_2-SiO_2) are characterized by a particularly weak adhesion (0.3-0.5 J/m^2). This questions the possibility of a practical fabrication of resistant coatings by zinc deposition on the bare silica surfaces.

In order to get a better insight into the process of siloxane breaking at the zinc/silica interface and to estimate the energy barrier between the two configurations we have used a 5-point climbing image nudged elastic band method[43]. We find that the interface reaction occurs in two steps, corresponding to the successive breaking of the two Si-O-Si bridges. Structural and energetic information concerning the first step of the reaction are summarized in Fig. 9. Starting from the D_2-SiO_2 configuration, the lower Si-O-Si bridge of the siloxane ring is first broken. The bridge anion (labeled 2 in Fig. 9) shifts towards a sub-surface Si, which repels one of the Si anion neighbor (labeled 3) into the interface. The resulting under-coordination of anion #3 enables the formation of two new strong Zn-O bonds per unit cell. Interestingly, this configuration is nearly iso-energetic with the SiO_2 one in Fig.6, where the siloxane ring is fully broken and four Zn-O bonds per unit cell are formed. This shows that the cost of one Si-O bond is approximately equal to that of two Zn-O bonds. Most importantly, we find that the first step of siloxane breaking requires to overcome a nearly 2 eV-high energy barrier, suggesting that an efficient ring breaking occurs only under extremely high temperature conditions, which may be not compatible with the stability of the zinc deposit itself. As a consequence, zinc deposition at the most stable bare D_2-SiO_2 silica surfaces is unlikely to produce cohesive interfaces, consistently with the observed detrimental effect of surface silica formation on galvanic zinc coatings of industrial high strength steels.

Before concluding, let us note that the overall pattern of zinc interaction at various terminations of silica shows clear similarities with zinc interaction at the α-alumina(0001) surfaces[44]. This suggests that, similarly to the case of alumina, adhesion improvement of zinc/silica interfaces may require the presence of interfacial buffers made of more reactive elements[45–47]. However, we stress that surface siloxane rings, which are a structural peculiarity of the non-polar silica surfaces, may require specific treatment to break them. From this point of view, surface prehydroxylation[48] appears as a particularly promising lever due to the known capacity of surface hydroxyls to break surface siloxane rings. Alternative routes of adhesion improvement are presently under study in our group.

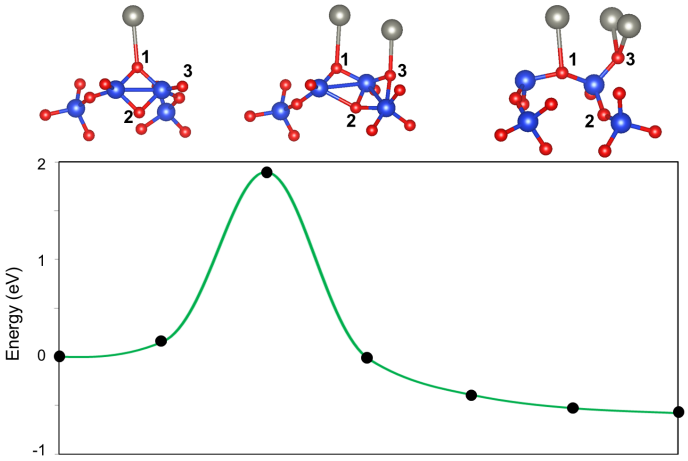

Fig. 9 Energy barrier for breaking the siloxane ring at the non-polar (001) zinc/silica interface and the corresponding initial, transition, and final configurations. Only the interface Si, Zn and O atoms directly involved in the process are shown with large blue, large gray, and medium red balls, respectively.

6 Conclusion

We have used ab initio modeling to analyze the interaction of zinc with silica surfaces, represented by various orientations [(001) and (111)] and terminations (polar or non-polar) of β-cristobalite.

We find that, regardless their orientation, polarity is the key factor which drives the main structural, electronic, and stability characteristics of the bare silica surfaces. The energy cost of polarity compensation makes polar terminations systematically less stable under accessible oxygen conditions, while non-polar surfaces are additionally stabilized by the formation of surface siloxane rings. Our results show that the characteristics of these siloxane groups depend relatively little on the surface orientation and the local surface structure, which makes them representative also for similar surface sites at amorphous silica surfaces.

Similarly, the characteristics of zinc/cristobalite interfaces depend relatively little on their orientation, but are very sensitive to the precise interface composition and structure. We find that the metal-oxide interaction at polar oxygen-rich interfaces is particularly strong thanks to the good screening capacity of zinc. Conversely, zinc interacts very weakly with surface siloxanes at non-polar interfaces and moderately strongly with the under-coordinated anions produced upon siloxane breaking. The different character and interaction strength at these two interfaces make the siloxane-containing interfaces less thermodynamically stable. In order to break an interface siloxane ring, we show that, despite the presence of zinc, a considerable energy barrier has to

be overcome.

This fundamental understanding of the microscopic mechanisms responsible for the interaction strength at zinc/silica interfaces under a large variety of oxidizing conditions provides several useful guidelines for possible adhesion improvement scenarios. In particular, it points out the unique and silica-specific role played by surface siloxane rings, the breaking of which is a prerequisite for any significant interaction improvement at non-polar interfaces.

7 Acknowledgments

The authors are grateful to Jacques Jupille, Rémi Lazzari, Lucie Gaouyat and Daniel Chaleix for many fruitful discussions, and to IDRIS for a generous allocation of computing time, under Project No. 100170. H.-L. T. Le acknowledges a post-doctoral grant from ArcelorMittal Maizières Research. This work was supported by French state funds within the framework of the Cluster of Excellence MATISSE led by Sorbonne Universités.

References

1 H.-T. Jiang, W. Ding, D. Tang and W. Huang, *J. Iron and Steel Research*, 2012, **19**, 29–36.

2 I. Nikulin, T. Sawaguchi and K. Tsuzaki, *Materials Science and Engineering A*, 2013, **587**, 192–200.

3 W. Wang, M. Li, C. He, X. Wei, D. Wang and H. Dub, *Materials and Design*, 2013, **47**, 510–521.

4 A. Mertens, E. M. Bellhouse and J. R. McDermid, *Materials Science & Engineering A*, 2014, **608**, 249–257.

5 A. R. Marder, *Prog. Mater. Sci.*, 2000, **45**, 191–271.

6 P. Drillet, Z. Zermout, D. Bouleau, J.-M. Mataigne and S. Claessens, *Rev. Metall.-Cah. Inf. Tech.*, 2004, **10**, 831–837.

7 C. Pesci, D. Chaleix, E. Silberberg and B. Chatelain, *Jet vapor deposition: coating steels of the future*, Paper presented at SCT2017 - 5th International Conference on Steels in Cars and Trucks, Amsterdam-Schiphol, The Netherlands, 2017.

8 C. Pesci, L. Diez, D. Chaleix, B. Chatelain and E. Silberberg, *Jet vapor deposition: coating steels of the future*, Paper presented at Galvatech 2017 - 11th International Conference on Zinc and Zinc Alloy Coated Steel Sheet, Tokyo, Japan, 2017.

9 C. T. Campbell, *Surface Science Reports*, 1997, **27**, 1–111.

10 Q. Fu and T. Wagner, *Surface Science Reports*, 2007, **62**, 431–498.

11 G. Bordier and C. Noguera, *Phys. Rev. B*, 1991, **44**, 6361–6371.

12 J. Goniakowski and C. Noguera, *Interface Science*, 2004, **12**, 93–103.

13 J. Goniakowski, C. Mottet and C. Noguera, *physica status solidi (b)*, 2006, **243**, 2516–2532.

14 M. V. Koudriachova, J. V. L. Beckers and S. W. de Leeuw, *Comp. Mater. Sci.*, 2001, **20**, 381–386.

15 E. Chagarov, A. A. Demkov and J. B. Adams, *Phys. Rev. B*, 2005, **71**, 075417.

16 F. Vigné-Maeder and P. Sautet, *J. Phys. Chem. B*, 1997, **101**, 8197–8203.

17 X. Rozanska, F. Delbecq and P. Sautet, *Phys. Chem. Chem. Phys.*, 2010, **12**, 14930–14940.

18 D. Ceresoli, M. Bernasconi, S. Iarlori, M. Parrinello and E. Tosatti, *Phys. Rev. Lett.*, 2000, **84**, 3887–3890.

19 K. Nagao, J. B. Neaton and N. W. Ashcroft, *Phys. Rev. B*, 2003, **68**, 125403.

20 E. A. A. Jarvis and E. A. Carter, *J. Am. Ceram. Soc.*, 2003, **86**, 373–386.

21 B. Magyari-Kope, S. Park, L. Colombo, Y. Nishi and K. Cho, *J. Appl. Phys.*, 2009, **105**, 013711.

22 P. N. Plessow, R. S. Sanchez-Carrera, L. Li, M. Rieger, S. Sauer, A. Schaefer and F. Abild-Pedersen, *J. Phys. Chem. C*, 2016, **120**, 10340–10350.

23 D. Ricci and G. Pacchioni, *Phys. Rev. B*, 2004, **69**, 161307(R).

24 D. E. Jiang and E. A. Carter, *Phys. Rev. B*, 2005, **72**, 165410.

25 G. Kresse and J. Furthmuller, *Phys. Rev. B*, 1996, **54**, 11169–11186.

26 G. Kresse and J. Hafner, *Phys. Rev. B*, 1993, **47**, 558–561.

27 P. E. Blöchl, *Phys. Rev. B*, 1994, **50**, 17953–17979.

28 G. Kresse and J. Joubert, *Phys. Rev. B*, 1999, **59**, 1758–1775.

29 M. Dion, H. Rydberg, E. Schroder, D. C. Langreth and B. I. Lundqvist, *Phys. Rev. Lett.*, 2004, **92**, 246401.

30 J. Klimes, D. R. Bowler and A. Michaelides, *J. Phys.: Cond. Matt.*, 2010, **22**, 022201.

31 J. Klimes, D. R. Bowler and A. Michaelides, *Phys. Rev. B*, 2011, **83**, 195131.

32 R. F. W. Bader, *Chem. Rev.*, 1991, **91**, Chem. Rev.

33 G. Henkelman, A. Arnaldsson and H. Jonsson, *Comput. Mater. Sci.*, 2006, **36**, 354–360.

34 K. Momma and F. Izumi, *J. Appl. Crystallogr.*, 2011, **41**, 1272–1276.

35 T. Demuth, Y. Jeanvoine, J. Hafner and J. G. Angyan, *J. Phys.: Condens. Matter*, 1999, **11**, 3833.

36 J. D. Cox, D. D. Wagman and V. A. Medvedev, *CODATA Key Values for Thermodynamics*, Hemisphere Publishing Corp., New York, 1984.

37 M. W. C. Jr., *J. Phys. Chem. Ref. Data*, 1998, **Monograph 9**, 1–1951.

38 J. Goniakowski, F. Finocchi and C. Noguera, *Rep. Prog. Phys.*, 2008, **71**, 016501.

39 J. Neugebauer and M. Scheffler, *Phys. Rev. B*, 1992, **46**, 16067–16080.

40 B.C.Bunker, D.M.Haaland, K.J.Ward, T.A.Michalske, W.L.Smith, J.S.Binkley, C.F.Melius and C.A.Balfe, *Surf. Sci.*, 1989, **210**, 406–428.

41 A. Grabbe, T. A. Michalske and W. L. Smith, *J. Phys. Chem.*, 1995, **99**, 4648–4654.

42 S. Iarlori, D. Ceresoli, M. Bernasconi, D. Donadio and M. Parrinello, *J. Phys. Chem. B*, 2001, **105**, 8007–8013.

43 G. Henkelman, B. Uberuaga and H. Jonsson, *J. Chem. Phys.*, 2000, **113**, 9901–9904.

44 R. Cavallotti, J. Goniakowski, R. Lazzari, J. Jupille, A. Koltsov and D. Loison, *J. Phys. Chem. C*, 2014, **118**, 13578–13589.

45 R. Cavallotti, H.-L. T. Le, J. Goniakowski, R. Lazzari, J. Jupille, A. Koltsov and D. Loison, *Phys. Chem. Chem. Phys.*, 2016, **18**, 3032–3039.

46 H.-L. T. Le, J. Goniakowski, C. Noguera, A. Koltsov and J.-M. Mataigne, *J. Phys. Chem. C*, 2016, **120**, 9836–9844.

47 H.-L. T. Le, J. Goniakowski, C. Noguera, A. Koltsov and J.-M. Mataigne, *J. Phys. Chem. C*, 2017, **121**, 25143–25151.

48 H.-L. T. Le, R. Lazzari, J. Goniakowski, R. Cavallotti, S. Chenot, C. Noguera, J. Jupille, A. Koltsov and J.-M. Mataigne, *J. Phys. Chem. C Letters*, 2017, **121**, 11464–11471.